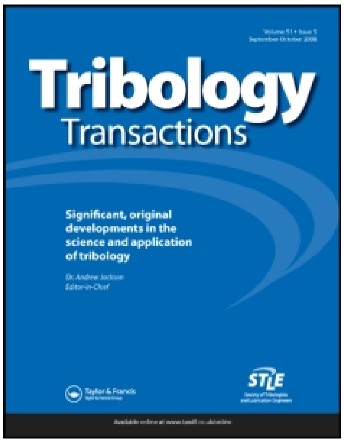

Tribology Transactions
Publication details, including instructions for authors and subscription information:
http://www.informaworld.com/smpp/title~content=t713669620

Empirical Stress Intensity Factors for Surface Cracks under Rolling Contact Fatigue

George Levesque[a]; Nagaraj K. Arakere[a]
[a] Department of Mechanical and Aerospace Engineering, University of Florida, Gainesville, FL

First published on: 23 July 2010

Tribology Transactions, 53: 621-629, 2010

ISSN: 1040-2004 print / 1547-397X online
DOI: 10.1080/10402001003642759

Empirical Stress Intensity Factors for Surface Cracks under Rolling Contact Fatigue

GEORGE LEVESQUE and NAGARAJ K. ARAKERE
Department of Mechanical and Aerospace Engineering
University of Florida
Gainesville, FL 32611-6300

This article contains empirical equations for the K_I, K_{II}, and K_{III} stress intensity factors (SIFs) for semi-elliptical surface cracks for brittle materials subjected to rolling contact fatigue (RCF) as a function of the contact patch diameter, angle of crack to the surface, max pressure, position along the crack front, and aspect ratio of the crack. The equations were developed from SIFs calculated by parametric three-dimensional (3D) finite element analysis (FEA) for a range of contact patch radii (1b, 2b, and 3b) and angles of the crack to the surface (0°, 45°, and 60°). Calculating mixed-mode SIFs for surface cracks subject to RCF using 3D FEA is computationally complex because of extreme mesh refinement required at multiple levels to capture steep stress gradients. The comprehensive empirical curve fits presented are accurate to within 0.5% of FE simulations and are useful for component design where contact-initiated surface fatigue damage is important such as in gears, roller bearings, and railway wheels. The results are of particular relevance to hybrid silicon nitride ball bearings, which are susceptible to failure from fatigue spalls emanating from pre-existing surface cracks, due to crack growth driven by RCF (G. Levesque and N. K. Arakere, An investigation of partial cone cracks in silicon nitride balls. International Journal of Solids and Structures, 2008, 45:6301–6315).

KEY WORDS

Ball Bearings; Ceramics; Semi-Elliptical Crack; Contact Mechanics; Fatigue Crack Propagation; Rolling Contact Fatigue; Stress Analysis; Finite Element Analysis; Stress Intensity Factor; Silicon Nitride Balls

INTRODUCTION

Surface cracks are among the most common flaws and most critical (Evans *(1)*; Hadfield, et al. *(2)*) in mechanical components and are directly exposed to rolling contact fatigue (RCF) in multiple systems. The RCF life of hybrid silicon nitride (Si_3N_4) ball/steel raceway bearings was found to be over twice that of steel bearings (Miner, et al. *(3)*; Tanimoto, et al. *(4)*). However, silicon nitride has low fracture toughness and failures of Si_3N_4 balls originate from small surface defects and cracks arising from the manufacturing processes (Wang, et al. *(4)*; Piotrowski *(6)*). These surface flaws are the most common source of ball failure in silicon nitride hybrid-bearing systems (Hadfield, et al. *(2)*; Levesque and Arakere *(7)*). Stress intensity factors (SIFs) have been the primary tool for analysis of growth and fracture propagating from these flaws. Due to the complexity of the three-dimensional (3D) subsurface Hertzian stress field at the ball–raceway interface and the steep stress gradients from the edge of contact and from the surface crack, exact solutions are intractable. Accounting for these complexities entails the use of a comprehensive 3D finite element contact/fracture mechanics analysis. Previous researchers have only provided a limited number of approximations for SIFs for this system. A brief review follows.

In earlier works, where the investigated geometries had similar levels of complexity to the current work, finite element analysis (FEA) was not always used. Zalounia *(8)* used the Fourier transform method to obtain SIFs for an edge crack penetrating the interface in a coated solid subjected to contact loading. Keer and Bryant *(9)* used two-dimensional (2D) linear elastic theory to simulate a crack in a rail wheel to examine the effects of contact friction, lubricant pressure, and friction between the crack faces on the K_I and K_{II} stress intensity factors. Karapetian and Hanson *(10)* derived weight equations for the simpler geometry of a submerged circle crack subjected to point loads on the crack face. Later, these equations would be applied by Kida and Ogura *(11)* (with some untested approximations) to the case of a subsurface penny crack subjected to RCF at the surface. Hasebe and Qian *(12)–(15)* visited the problem of an indenter of different geometries contacting a plane strain infinite plate with an angled surface flaw in multiple notable works by using complex stress functions derived by the rational mapping function. The results presented were in graphical form and not readily applicable to a 3D problem.

Noda and Miyoshi *(16)* used the body force method to come up with an integral equation that could be integrated with a polynomial stress distribution for a half penny crack in a semi-infinite body. Pommier, et al. *(17)*, in a related work on semi-elliptical cracks that are normal to the surface, provided a set of equations

Manuscript received July 10, 2009
Manuscript accepted December 14, 2009
Review led by Bob Errichello

NOMENCLATURE

a = Depth of crack along its face
a_i = Coefficients of a polynomial for K_I
b = Semi-width of crack on the surface
b_i = Coefficients of a polynomial for K_{II}
c_i = Coefficients of a polynomial for K_{III}
E = Young's modulus
K_i^* = $\frac{K_i}{p_o\sqrt{\pi\frac{a}{Q}}}$ where $i = I, II, III$
K_I = Mode I stress intensity factor
K_{II} = Mode II stress intensity factor
K_{III} = Mode III stress intensity factor
p_o = Peak contact pressure
Q = Shape factor for elliptical crack
R = $\sqrt{x^2+y^2}$
r = Radius of contact patch expressed as $1b$, $2b$, $3b$
v = Poisson's ratio
u_i, v_i, w_i = Displacements of crack face nodes in the mode I, II, and III directions
x_d = Distance between crack and load edge
θ = Angle of crack inclination toward the vertical
ϕ = Position along crack front

for K_I for a polynomial stress distribution that could be explained by the equation:

$$\sigma_{xx} = \sigma\left(\frac{x}{a}\right)^m\left(\frac{y}{b}\right)^n \qquad [1]$$

where the stress state is normal to the crack and n and m are constants whose sum is less than 4.

Kaneta and Murakami *(18)* investigated the penny crack by using the body force method. Their mode I SIFs occasionally went negative, due to a neglect of crack closure, when the contact patch started to go over the load. Kaneta, et al. *(19)* also visited the problem of an inclined subsurface penny crack subjected to line contact loading to investigate subsurface crack growth under RCF.

FEA would also be used for analysis for a similar family of crack problems. Komvopoulos and Cho *(20)* used 2D FEA to simulate a subsurface plane strain crack that was parallel to the surface under sliding asperity contact. Zhang, et al. *(21)* also used FEA but for the analysis of two vertical surface cracks under contact loading in 2D. Kojima *(22)* used 2D FEA to analyze the angled surface crack under contact loading with a viscous lubricant to penetrate the crack. For the case of cone cracks with an internal circularly symmetric load, FEA was used to find the worst "crack angle" and the "critical flaw" size as determined by what causes the SIFs to reach the K_{eff} to initiate fatigue (Warrier, et al. *(23)*).

Fletcher and Beynon *(24)*, *(25)* applied their work to calculating SIFs for the specific case of contact loading for inclined cracks. Their method for calculating SIFs involved edge Green's functions presented graphically in the works of Rooke, et al. *(26)*, which must then be integrated based on the amount of crack opening. The method uses an approximation of an infinitely wide crack to calculate SIFs for the deepest point of a semicircular surface crack. Problematically, this point may not be where the highest SIFs occur along the crack front depending on the depth of the crack (Newman and Raju *(27)*).

Reflecting on these prior works, we see some limitations in applying them to practical RCF problems. Real RCF produces a complex stress field that is not easily characterized by many of the above methods. In many cases K_I is sometimes supplied as a negative number, which, though physically impossible, has often gone unmentioned; that is, effects of crack closure have been ignored. If K_I is supplied, K_{II} or K_{III} may not be supplied even though all modes of crack tip deformation are present and contributing to mixed-mode crack growth. Also, the problem requires a 3D analysis, which rules out much of the prior work. Beyond this, previous results were often not generalized and case specific. The preexisting surface flaws present in silicon nitride balls are typically partial cone cracks or c-cracks (Hadfield, et al. *(2)*) and their 3D crack geometry was described by Levesque and Arakere *(7)*. The c-cracks have nonplanar crack faces but also possess nonplanar crack tips, making their shape more difficult to describe and therefore more difficult to analyze in any linear elastic fracture mechanics (LEFM)-based analysis. In this work, we present comprehensive results for the calculation of SIFs for semi-elliptical cracks in brittle materials under RCF. In a follow-up article (Levesque and Arakere *(28)*), we will present a comparison of SIFs for partial cone or c-cracks and semi-elliptical cracks subject to circular and elliptical RCF that shows that use of semi-elliptical crack with circular contact leads to conservative estimates for SIFs and critical flaw size, required for defining limits for nondestructive evaluation methods for silicon nitride ball quality control. The results generated are of immediate engineering relevance to the hybrid ball bearing industry toward evaluating critical flaw size (Levesque and Arakere *(28)*) and for developing a fracture mechanics–based life prediction methodology for hybrid bearings. The empirical curve fits will also be of relevance to other areas of component design where contact-initiated fatigue damage is important, such as gears, roller bearings, and railway wheels.

ANALYSIS

A detailed investigation of SIFs for a semi-elliptical flaw under rolling contact fatigue can only be properly done in 3D. This implies a 3D FEA analysis, as any analytical method would quickly become intractable under this complex stress state. We have modeled the semi-elliptical crack for different aspect ratios, orientations of load, radius of load, and angles to the surface. The resulting trends are plotted and are fitted to equations for ease of use.

The FEA model has been created using either FRANC3D/NG, as developed by the Fracture Analysis Consultants *(29)* or ABAQUS (Desault Systemes *(30)*). FRANC3D/NG makes it easier for the user to create meshes of cracked bodies with limited control of the mesh density. The mesh density is critical for both the accurate calculation of the crack tip opening displacements and for capturing the stress gradients of the Hertzian contact.

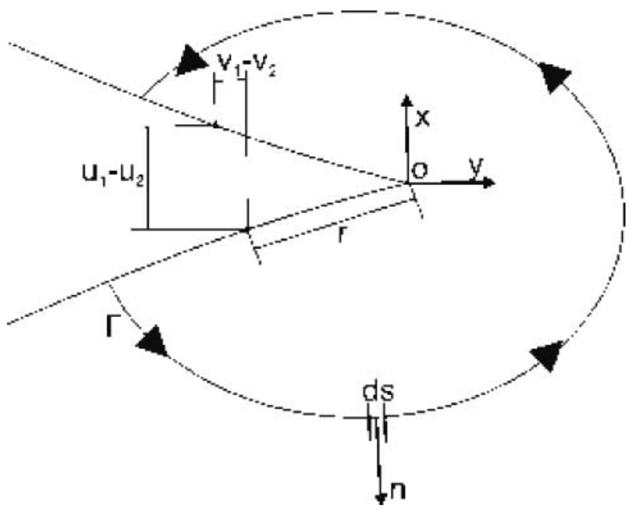

Fig. 1—Illustration of contour integral and displacement correlation variables in the neighborhood of a two-dimensional crack.

SIF extraction from the FE crack mesh is feasible through a few methods such as stress matching (Anderson *(31)*) and virtual crack extension (Anderson *(31)*), but the most appropriate approach for our analyses is via crack tip opening displacement (CTOD) correlation because it accounts for the effects of all physical phenomena (Aliabadi and Rooke *(32)*). The J-integral implementation in commercial codes has yet to adequately account for traction arising from crack face contact during closure. Rice's *(33)* J-integral formulation is given by

$$J = \int_{\Gamma} w dy - T_i \frac{\partial u}{\partial x} ds \qquad [2]$$

where the variables are defined in Fig. 1. The traction term, T_i, is not evaluated in ABAQUS v. 6.7-1 (Desault Sytemes *(30)*) even if contact elements are used on the crack faces to discern closure and traction forces.[1] To avoid errors from this issue, in this instance, it is convenient to resort to CTOD correlation for computing SIFs, rather than use J-integral decomposition or the M-integral in FRANC3D/NG (Bank, et al. *(34)*). The intricacies of evaluating SIFs for 3D surface cracks subject to RCF including effects of crack closure and traction are covered in detail in a companion paper by Levesque and Arakere *(28)*. The SIFs are calculated by using a displacement correlation technique as described by the equations:

$$K_I = \frac{E}{4(1-\nu^2)}\sqrt{\frac{2\pi}{r}}\,(u_1 - u_2) \qquad [3]$$

$$K_{II} = \frac{E}{4(1-\nu^2)}\sqrt{\frac{2\pi}{r}}\,(v_1 - v_2) \qquad [4]$$

$$K_{III} = \frac{E}{4(1-\nu^2)}\sqrt{\frac{2\pi}{r}}\,(w_1 - w_2) \qquad [5]$$

Quadratic elements are required by the displacement correlation method for calculating SIFs because the insertion of a quarter point element greatly increases the accuracy of the model without a dramatic increase in mesh density. To reduce the size of the problem we utilize a technique referred to as *submodeling*, where we apply displacements to the boundary of a small cracked block to simulate its being a part of a much larger half-space (Desault Systemes *(30)*). The contact load is applied to the surface with FORTRAN user subroutines DLOAD (and UTRACLOAD) for ABAQUS (see Fig. 2). We apply this load up until the edge of the crack but not over the crack, because this would cause the applied pressure to be inaccurate (Rice *(33)*). Also, crack closure would result (Fujimote, et al. *(35)*) and the model would then require a contact algorithm on an already large fracture model with quadratic elements that would be accurate enough to yield crack tip displacements.

1 The neglect of the traction term for contacting crack faces is not mentioned in Desault Ssytemes *(30)*.

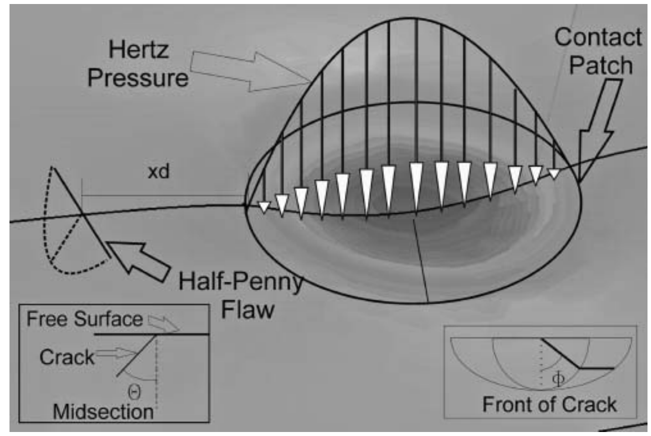

Fig. 2—Model configuration displaying orientation of load and defining variables θ, ϕ, and x_d.

Crack Geometry

Surface cracks can have a variety of shapes. Cone cracks have received much attention in the literature (Mackerle *(36)*). Partial cone cracks are reviewed in separate papers by Levesque and Arakere (*7*), *(28)* and have also been the subject of some analyses (Hadfield, et al. *(2)*, *(37)*; Wang and Hadfield *(38)*; Zhao, et al. *(39)*). Penny cracks seem to be the simplest to mesh and simulate in a 3D FEA analysis. Additionally, we have shown that penny cracks subject to circular RCF result in the highest SIFs (Levesque and Arakere *(28)*).

However, if we were to limit our attention to the family of possible half-penny surface flaws, we are left with only two features that can be altered, aspect ratio and angle toward the surface. We have analyzed five aspect ratios ($a/b = 0.2$, 0.4, 0.6, 0.8, and 1) under three different angles ($\theta = 0^\circ$, 45°, and 60°).

Orientation of Load

As a surface flaw is subjected to RCF, a load is set in a direction across the free surface of the cracked body. In application, this pass of a load will happen repeatedly, subjecting the part to cyclic loading. As the load is approaching the load's relative orientation generates a different set of SIFs at each instant, there is one orientation (for a given load size and magnitude) that produces the highest SIFs along the crack front. It is this orientation

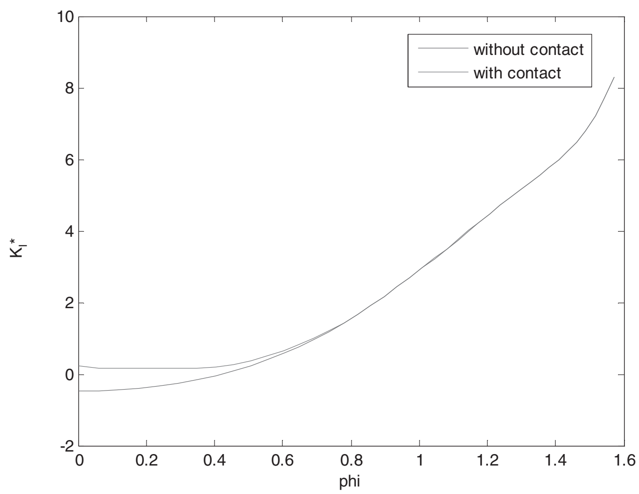

Fig. 3—K_I for a single load geometry with and without contact defined.

TABLE 1—THE DISTANCES IN UNITS OF b (THE CRACK SEMI-WIDTH) FROM THE CRACK ON THE SURFACE, TO THE CONTACT PERIPHERY WHERE THE K_I WAS FOUND TO REACH A MAXIMUM

$r =$	$1b$	$2b$	$3b$
$\theta = 0°, a/b = 1.0$	1.3	1.0	0.875
$\theta = 0°, a/b = 0.8$	1.3	0.875	0.875
$\theta = 0°, a/b = 0.6$	1.1	0.875	0.875
$\theta = 0°, a/b = 0.4$	0.95	0.625	0.75
$\theta = 0°, a/b = 0.2$	0.95	0.625	0.625
$\theta = 45°, a/b = 1.0$	1.0	0.625	0.5
$\theta = 45°, a/b = 0.8$	1.25	0.5	0.5
$\theta = 45°, a/b = 0.6$	1.25	0.5	0.5
$\theta = 45°, a/b = 0.4$	1.25	0.5	0.375
$\theta = 45°, a/b = 0.2$	1.25	0.5	0.375
$\theta = 60°, a/b = 1.0$	0.0	0.0	0.0
$\theta = 60°, a/b = 0.8$	0.0	0.0	0.0
$\theta = 60°, a/b = 0.6$	0.0	0.0	0.0
$\theta = 60°, a/b = 0.4$	0.0	0.0	0.0
$\theta = 60°, a/b = 0.2$	0.0	0.0	0.0

that is of most interest for a design analysis that would determine whether the SIFs reach a critical value to induce fracture, K_c; initiate fatigue, K_{eff}; or will direct a growth analysis, ΔK_{eff}.

In some orientations of load, the crack faces interpenetrated when contact was not defined, indicating that crack closure occurred. The interpenetration resulted in a negative K_I stress intensity factor but K_{II} and K_{III} remained identical. Figure 3 compares K_I along the crack front, with and without contact defined. Reflection indicates that simply setting the $K_I = 0$ when $K_I < 0$ is conservative under conditions of crack closure. It must be noted that the coefficient of friction for contact elements between the crack faces was set to zero. For non-zero friction between the crack faces it is possible that closure might couple modes of deformation. Herein, we have implemented displacement correlation and this procedure will be discussed in a future work on modeling concerns for these types of problems.

Though the tensile region is maximal on the periphery of the contact patch in an uncracked body (according to the stress solution) this does not necessarily mean that this same position is where the maximum SIFs will occur. So, to find the worst-case load orientation we perturbed the distance between the contact patch edge and the crack center at the surface and calculated Ks for these orientations. The SIFs of multiple contact patch positions relative to the crack were compared and the highest SIFs were chosen for curve fitting. These distances for each model are given in Table 1. We noticed that this distance tends to decrease as load size is increased and as crack aspect ratio decreases (and the crack tip is generally closer to the surface) for the more vertical cracks (because this allows their tip to be more generally located in the small tensile region about the contact).

Load

RCF can have multiple different shapes of pressure distribution, but if the two contacting bodies can be characterized with two radii of curvature each, as in a Hertzian contact, then the contact patch will be elliptical. For bodies whose radii of curvature are identical the contact patch is circular and its pressure distribution is

$$P(x, y) = p_o\sqrt{1 - R^2} \quad [6]$$

It is important to note that the radial tensile stress region at the edge of contact is both small and quickly decays with increasing depth into the material. Also, the decay of the stress clearly shows that the stress state is quite far from anything that can be considered as far-field. The absence of a clearly identifiable far-field stress seen by the crack makes the curve fits more complicated than those employed by the widely referenced paper by Newman and Raju *(27)*.

We provide empirical equations for circular loading of penny cracks at a few angles. The range of size of circular loads has been nondimensionalized with respect to the crack half-width and has been analyzed for the $r = 1b$, $2b$, and $3b$ cases, which we feel should cover the majority of cases that would be of engineering interest. The data obtained from FEA were fit to the equations:

$$K_I = p_o\left(a_1 + a_2x + a_3x^2 + a_4x^3 + a_5x^4\right) gf_\phi\sqrt{\pi\frac{a}{Q}} \quad [7]$$

$$K_{II} = p_o\left(b_1 + b_2x + b_3x^2 + b_4x^3 + b_5x^4\right) gf_\phi\sqrt{\pi\frac{a}{Q}} \quad [8]$$

$$K_{III} = p_o\left(c_1 + c_2x + c_3x^2 + c_4x^3 + c_5x^4\right) gf_\phi\sqrt{\pi\frac{a}{Q}} \quad [9]$$

In this way, the results can be easily fit with very little error (~0.5%) by varying the polynomial coefficients a_i, b_i, and c_i and can be easily nondimensionalized. We note that when $a/b \leq 1$, Q is approximated by the equation:

$$Q = 1 + 1.464\left(\frac{a}{b}\right)^{1.65} \quad [10]$$

Also,

$$g = 1 + 0.1(1 - \sin\phi)^2 \quad [11]$$

$$f_\phi = \left[\left(\frac{a}{b}\right)^2\cos^2\phi + \sin^2\phi\right]^{\frac{1}{2}} \quad [12]$$

TABLE 2—COEFFICIENTS FOR ALL PARAMETRIC CASES FOR K_I, K_{II}, AND K_{III} FOR $\theta = 0°$

$\theta = 0°$	a/b	r	a_5	a_4	a_3	a_2	a_1
K_I	1	1b	0.00057	−0.00152	0.00233	−0.00027	0.00209
		2b	0.00160	−0.00449	0.00743	−0.00082	0.00529
		3b	0.00326	−0.00928	0.01603	−0.00172	0.01017
	0.8	1b	0.00631	−0.00882	0.00516	−0.00059	0.00240
		2b	0.01813	−0.02534	0.01571	−0.00173	0.00654
		3b	0.03734	−0.05212	0.03330	−0.00359	0.01313
	0.6	1b	0.01528	−0.02003	0.00842	−0.00108	0.00250
		2b	0.04472	−0.05859	0.02521	−0.00318	0.00712
		3b	0.09423	−0.12337	0.05377	−0.00671	0.01478
	0.4	1b	0.01711	−0.02316	0.00882	−0.00120	0.00232
		2b	0.05121	−0.06928	0.02663	−0.00361	0.00688
		3b	0.10771	−0.14566	0.05629	−0.00760	0.01439
	0.2	1b	−0.00905	0.00734	−0.00285	0.00021	0.00181
		2b	−0.02741	0.02232	−0.00860	0.00063	0.00546
		3b	−0.05815	0.04745	−0.01823	0.00135	0.01153
$\theta = 0°$	a/b	r	b_5	b_4	b_3	b_2	b_1
K_{II}	1	1b	−0.00005	0.00059	−0.00135	0.00011	0.00043
		2b	−0.00011	0.00167	−0.00400	0.00030	0.00130
		3b	−0.00027	0.00369	−0.00867	0.00063	0.00286
	0.8	1b	0.00167	−0.00220	−0.00033	−0.00009	0.00027
		2b	0.00517	−0.00691	−0.00083	−0.00031	0.00078
		3b	0.01093	−0.01453	−0.00185	−0.00065	0.00167
	0.6	1b	0.00260	−0.00398	0.00072	−0.00020	0.00015
		2b	0.00788	−0.01206	0.00224	−0.00062	0.00042
		3b	0.01667	−0.02550	0.00476	−0.00132	0.00086
	0.4	1b	−0.00058	−0.00043	−0.00017	−0.00006	0.00007
		2b	−0.00190	−0.00114	−0.00055	−0.00018	0.00018
		3b	−0.00423	−0.00215	−0.00124	−0.00036	0.00037
	0.2	1b	−0.00502	0.00535	−0.00209	0.00023	0.00001
		2b	−0.01555	0.01661	−0.00647	0.00071	0.00003
		3b	−0.03324	0.03555	−0.01384	0.00152	0.00006
$\theta = 0°$	a/b	r	c_5	c_4	c_3	c_2	c_1
K_{III}	1	1b	−0.00072	0.00206	−0.00129	−0.00047	−0.00003
		2b	−0.00215	0.00613	−0.00383	−0.00136	−0.00009
		3b	−0.00457	0.01299	−0.00804	−0.00290	−0.00019
	0.8	1b	−0.00349	0.00719	−0.00367	−0.00026	−0.00002
		2b	−0.01045	0.02144	−0.01095	−0.00071	−0.00007
		3b	−0.02215	0.04527	−0.02312	−0.00145	−0.00015
	0.6	1b	−0.00218	0.00543	−0.00275	−0.00041	−0.00001
		2b	−0.00651	0.01619	−0.00823	−0.00121	−0.00004
		3b	−0.01380	0.03416	−0.01738	−0.00250	−0.00009
	0.4	1b	0.00440	−0.00286	0.00054	−0.00079	0.00000
		2b	0.01361	−0.00898	0.00172	−0.00242	−0.00001
		3b	0.02883	−0.01913	0.00369	−0.00510	−0.00001
	0.2	1b	0.01197	−0.01271	0.00448	−0.00119	0.00001
		2b	0.03696	−0.03926	0.01385	−0.00369	0.00004
		3b	0.07848	−0.08338	0.02941	−0.00783	0.00009

TABLE 3—COEFFICIENTS FOR ALL PARAMETRIC CASES FOR K_I, K_{II}, AND K_{III} FOR $\theta = 45°$

$\theta = 45°$	a/b	r	a_5	a_4	a_3	a_2	a_1
K_I	1	1b	0.03069	−0.06817	0.05008	−0.01249	0.00783
		2b	0.05798	−0.12787	0.10044	−0.02374	0.01392
		3b	0.06165	−0.13609	0.11087	−0.02560	0.02027
	0.8	1b	0.25896	−0.37265	0.16790	−0.02668	0.00796
		2b	0.47901	−0.68372	0.32295	−0.04879	0.01569
		3b	0.50815	−0.72296	0.34653	−0.05168	0.02271
	0.6	1b	0.01294	−0.01710	0.00755	−0.00106	0.00249
		2b	0.32412	−0.36314	0.13671	−0.01950	0.01478
		3b	0.12658	−0.08750	0.02082	−0.00246	0.02104
	0.4	1b	0.08439	−0.06357	0.00203	−0.00421	0.00718
		2b	0.14478	−0.15116	0.04963	−0.00780	0.01204
		3b	0.09795	−0.10360	0.03560	−0.00500	0.02300
	0.2	1b	0.02247	0.00565	−0.02538	−0.00281	0.00998
		2b	−0.01594	0.02200	−0.01337	−0.00007	0.01610
		3b	−0.03883	0.04039	−0.01662	0.00126	0.02068
$\theta = 45°$	a/b	r	b_5	b_4	b_3	b_2	b_1
K_{II}	1	1b	−0.02901	0.05987	−0.07188	0.01255	0.04438
		2b	−0.02804	0.06717	−0.09026	0.01562	0.05196
		3b	−0.02127	0.06061	−0.08914	0.01507	0.04856
	0.8	1b	−0.15705	0.17951	−0.14463	0.01446	0.04219
		2b	−0.08488	0.07200	−0.10265	0.00823	0.04500
		3b	0.00015	−0.02817	−0.05834	0.00234	0.03989
	0.6	1b	0.00480	−0.00766	0.00272	−0.00063	0.00019
		2b	0.97142	−1.49346	0.60414	−0.10156	0.03866
		3b	1.02226	−1.53021	0.62327	−0.10318	0.03278
	0.4	1b	−0.08691	0.12303	−0.13284	0.00258	0.02877
		2b	−0.01543	−0.05833	−0.02924	−0.00684	0.02684
		3b	0.05186	−0.12077	0.00423	−0.00754	0.01685
	0.2	1b	−0.17706	0.30827	−0.18665	0.00855	0.01485
		2b	0.06102	−0.06311	−0.02082	−0.00388	0.00863
		3b	0.12743	−0.16371	0.03198	−0.00820	0.00413
$\theta = 45°$	a/b	r	c_5	c_4	c_3	c_2	c_1
K_{III}	1	1b	−0.02890	0.10038	−0.09167	−0.00947	−0.00268
		2b	−0.02893	0.11510	−0.10462	−0.01713	−0.00316
		3b	−0.02652	0.10900	−0.09448	−0.01920	−0.00290
	0.8	1b	−0.09734	0.25130	−0.16807	−0.00512	−0.00214
		2b	−0.03831	0.21799	−0.16516	−0.01420	−0.00229
		3b	−0.01420	0.18514	−0.14208	−0.01526	−0.00202
	0.6	1b	0.00117	0.00032	−0.00057	−0.00048	−0.00001
		2b	0.10361	0.00956	−0.05369	−0.01667	−0.00096
		3b	0.04763	0.10309	−0.09433	−0.00746	−0.00105
	0.4	1b	0.25381	−0.26703	0.08972	−0.03561	−0.00028
		2b	0.39896	−0.42784	0.15003	−0.04753	−0.00017
		3b	0.56860	−0.61293	0.22239	−0.05780	0.00015
	0.2	1b	0.17767	−0.13319	0.05089	−0.05330	−0.00111
		2b	0.16738	−0.15268	0.04809	−0.03087	−0.00064
		3b	0.17233	−0.16379	0.05305	−0.02531	−0.00044

Though the fit uses components of the Newman and Raju *(27)* fit, it is more involved because of the complex 3D subsurface stress field and the steep stress gradients at the edge of contact to crack tip. The coefficients for these cases are provided in Tables 2–4.

RESULTS AND CONCLUSIONS

As a consequence of running these analyses for different aspect ratios and angles we can see a few notable trends as a result. Firstly, the location along the crack front where the SIFs are the highest can change based on crack depth and angle. Generally, the shallower cracks can have their SIFs toward the crack center, whereas the deeper cracks tend to have their SIFs highest near the surface.

For a single load size the worst-case crack is not obvious. Figures 4–6 provide K_I for each load size for all 15 modeled geometries. By reflecting on the results, we see that the $\theta = 45°$, $a/b = 1$ case has the highest SIFs for the $r = 2b$ and $3b$ cases.

TABLE 4—COEFFICIENTS FOR ALL PARAMETRIC CASES FOR K_I, K_{II}, AND K_{III} FOR $\theta = 60^\circ$

$\theta = 60^\circ$	a/b	r	a_5	a_4	a_3	a_2	a_1
K_I	1	1b	0.00022	0.00219	−0.00166	0.00151	0.01305
		2b	−0.00154	0.00912	−0.00541	0.00388	0.02207
		3b	−0.00407	0.01589	−0.00991	0.00569	0.02850
	0.8	1b	0.00580	0.00104	−0.00646	0.00132	0.01405
		2b	−0.00649	0.02848	−0.01860	0.00504	0.02342
		3b	−0.02152	0.05393	−0.03099	0.00769	0.02959
	0.6	1b	−0.00992	0.02657	−0.02304	0.00145	0.01485
		2b	−0.04943	0.07986	−0.04148	0.00617	0.02394
		3b	−0.07570	0.11359	−0.05482	0.00858	0.02964
	0.4	1b	0.19388	−0.20215	0.05007	−0.01112	0.01417
		2b	0.18599	−0.22079	0.07396	−0.01166	0.02164
		3b	0.12169	−0.15525	0.05367	−0.00837	0.02604
	0.2	1b	0.13338	−0.10915	0.00607	−0.00692	0.01262
		2b	0.08585	−0.09914	0.02550	−0.00562	0.01888
		3b	0.01541	−0.03383	0.00914	−0.00297	0.02266
$\theta = 60^\circ$	a/b	r	b_5	b_4	b_3	b_2	b_1
K_{II}	1	1b	−0.00062	−0.00185	−0.00699	−0.00085	0.01279
		2b	0.00082	−0.00312	−0.00757	−0.00122	0.00995
		3b	0.00176	−0.00287	−0.00670	−0.00122	0.00437
	0.8	1b	0.00520	−0.02522	−0.00543	−0.00325	0.01226
		2b	0.01770	−0.04188	0.00250	−0.00464	0.00800
		3b	0.02757	−0.04846	0.00790	−0.00505	0.00245
	0.6	1b	0.04532	−0.07520	0.00876	−0.00680	0.01044
		2b	0.04845	−0.08291	0.01570	−0.00701	0.00509
		3b	0.04929	−0.07602	0.01641	−0.00641	−0.00023
	0.4	1b	−0.15883	0.19031	−0.11165	0.00839	0.00678
		2b	0.11770	−0.17533	0.04090	−0.00955	0.00119
		3b	0.31135	−0.40073	0.13295	−0.02029	−0.00317
	0.2	1b	−0.36183	0.47099	−0.22470	0.02001	0.00731
		2b	−0.05244	0.05544	−0.05487	0.00289	0.00191
		3b	0.15749	−0.19656	0.04810	−0.00870	−0.00180
$\theta = 60^\circ$	a/b	r	c_5	c_4	c_3	c_2	c_1
K_{III}	1	1b	0.00218	−0.00133	0.00088	−0.01215	−0.00111
		2b	0.00378	−0.00180	0.00232	−0.01097	−0.00098
		3b	0.00263	0.00168	0.00087	−0.00567	−0.00056
	0.8	1b	0.03250	−0.03575	0.01271	−0.01721	−0.00131
		2b	0.04629	−0.04433	0.01722	−0.01513	−0.00107
		3b	0.03760	−0.02715	0.01109	−0.00829	−0.00060
	0.6	1b	0.06033	−0.05899	0.01928	−0.02105	−0.00187
		2b	0.06898	−0.05935	0.02020	−0.01772	−0.00148
		3b	0.05150	−0.03334	0.01189	−0.01070	−0.00087
	0.4	1b	0.37372	−0.38473	0.14244	−0.05317	0.00015
		2b	0.60388	−0.64698	0.23694	−0.05732	0.00054
		3b	0.59932	−0.63865	0.23462	−0.04821	0.00062
	0.2	1b	0.49753	−0.49000	0.18141	−0.06698	0.00012
		2b	0.82548	−0.87869	0.31396	−0.07222	0.00066
		3b	0.82666	−0.88589	0.31707	−0.06345	0.00078

In these situations, the highest SIFs occur near the free surface. For the $r = 1b$ case, the $\theta = 60^\circ$, $a/b = 0.2$ case has significantly higher K_{II} and K_{III} components and this occurs at the deepest portion of the crack. Neither of these observations is intuitive. In fact, they display that it is not always the steepest or the longest of cracks that will have the highest SIFs under a given load but rather an interesting combination thereof that varies with load size.

The variation of SIFs across the crack front also brings many issues in terms of crack growth. For example, if the highest SIFs are produced by a certain geometry crack and these SIF values are largest near the free surface, if this crack grows it

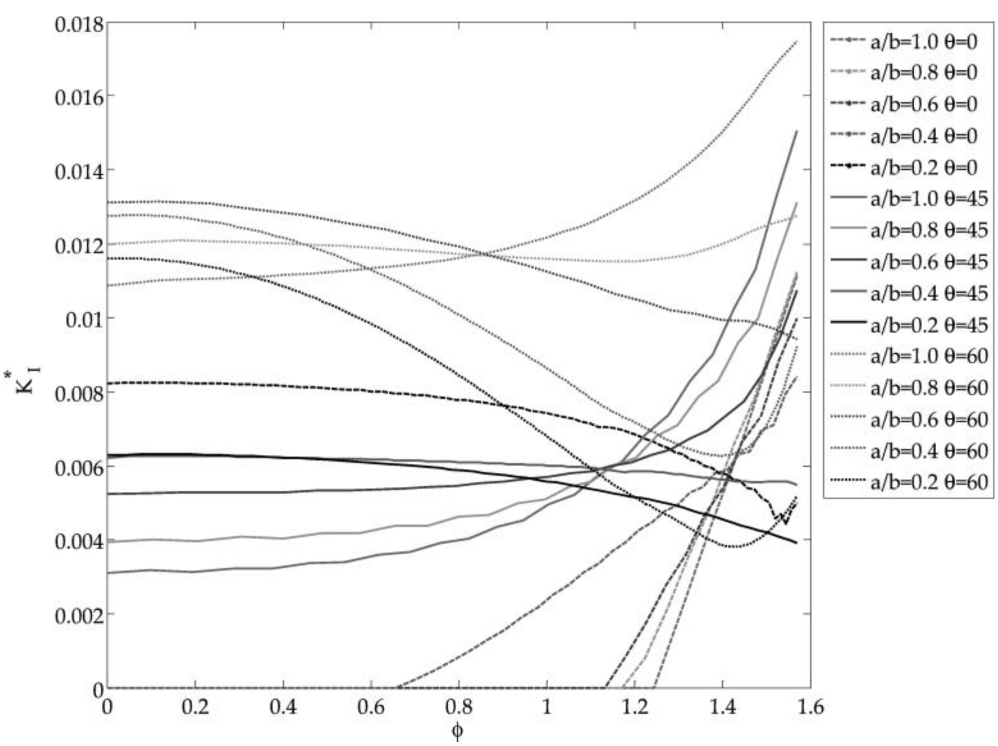

Fig. 4—K_I along the crack front for all variations of crack angle and depth for $r = 1b$.

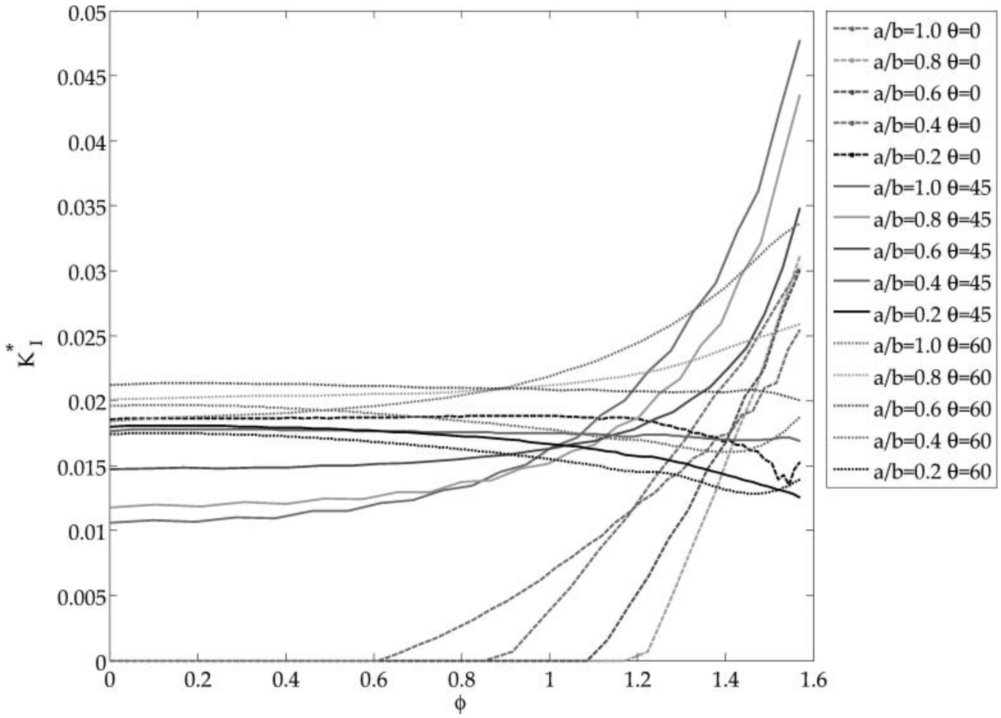

Fig. 5—K_I along the crack front for all variations of crack angle and depth for $r = 2b$.

will grow wider on the surface rather than into the depth. Then the geometry may become one that yields relatively lower SIFs than its former shape. This means the crack that produces the highest SIFs, for a given geometry and load, may not be the worst geometry crack under RCF because its shape evolution affects its SIFs and so the worst crack geometry is something that we intend to revisit in a future work.

Figures 4 to 6 contain every model created for each of the three types of load. The trends between models of the same angle but different depths are quite smooth and are reflective of

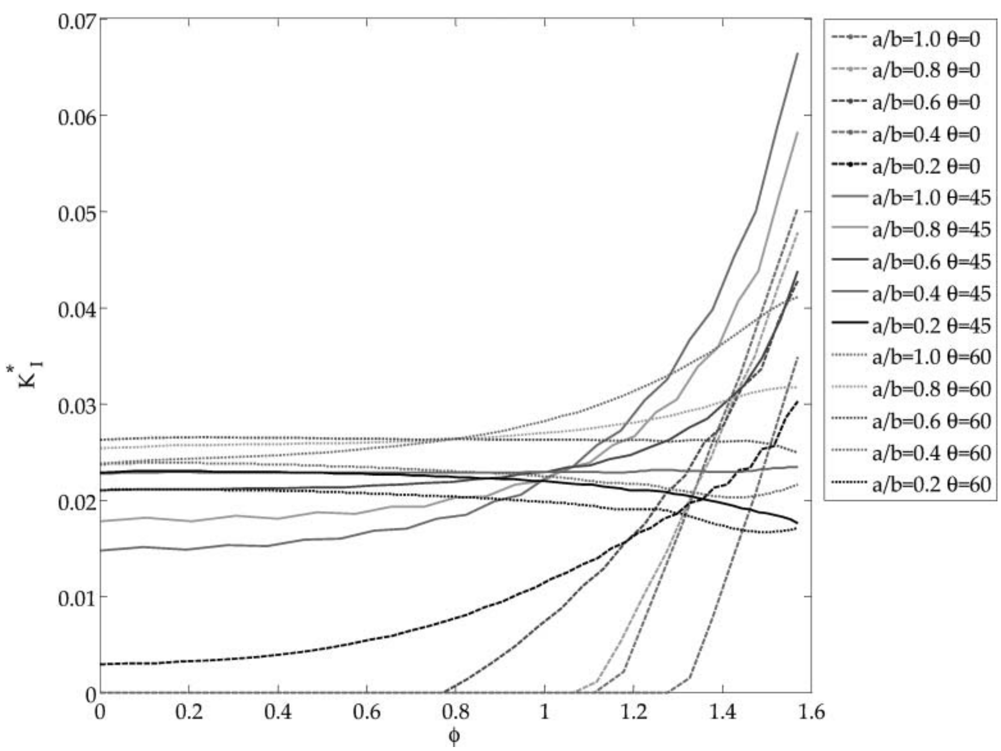

Fig. 6—K_I along the crack front for all variations of crack angle and depth for $r = 3b$.

the transitions of the stress state because a crack is longer. The trends between cracks of different angles are less obvious because the change in angle places the cracks in a different part of the stressed state. Quite surprisingly, the trends in $r = 3b$ seem smooth between all 15 models graphed even though the load orientation may not be identical for all models and the tip location may be quite different. This trend is observed because the larger contact patch produces lower stress gradients.

CONCLUSIONS

Three-dimensional FEA was performed on a parametric variation of semi-elliptical flaws under circular RCF patches to provide a set of comprehensive empirical equations for mixed-mode SIFs applicable in the hybrid ball bearing industry and other contact fatigue applications. Modeling concerns have been addressed and a modeling framework has been provided for analyzing surface cracks under RCF. The parametric variations of load size, crack angle, and crack depth displayed several interesting trends including the type of cracks that provide the highest SIFs for the given load geometry, which is neither the deepest crack nor the steepest crack all the time. The computational effort involved in evaluating mixed-mode SIFs for surface cracks subject to RCF are substantial because of multiple levels of mesh refinement required at the 3D contact and crack edge. The comprehensive and accurate (~0.5% error) empirical equations for the K_I, K_{II}, and K_{III} SIFs presented are of immediate engineering relevance to the hybrid silicon nitride ball bearing industry toward evaluating critical flaw size and for developing a fracture mechanics–based life prediction methodology. These curve fits are expected to have wider interest to other areas of component design where contact-initiated fatigue damage is important, such as gears, roller bearings, and railway wheels, and of general academic interest in fracture and contact mechanics.

ACKNOWLEDGMENTS

Robert Wolfe, Manager, Materials Technology, The Timken Company, Canton, Ohio, is thanked for extensive discussions on RCF loading of silicon nitride balls and design aspects of hybrid bearings. This work has been supported by The Timken Company, Canton, Ohio.

REFERENCES

(1) Evans, A. G. (1983), "Contact Stress at Ceramic Interfaces," in *Progress in Nitrogen Ceramics*, Riley, P. L. (Ed.), Martinus Nijhoff Publishers, Leyden, The Netherlands, p 595.

(2) Hadfield, M., Stolarski, T. A., Cundhill, R. T., and Horton, S. L. (1993), "Failure Modes of Ceramics in Rolling Contact," *Proceedings of the Royal Society of London - Series A*, **443**, pp 607-621.

(3) Miner, J. R., Dell, J., Galbato, A., and Ragen, M. A. (1996), "F-117-PW-100 Hybrid Bearing Ceramic Technology Insertion," *Journal of Engineering for Gas Turbines and Power*, **118**, pp 434-442.

(4) Tanimoto, K., Kajihara, K., and Yanai, K. (2000), "Hybrid Ceramic Ball Bearings for Turbochargers," **SAE Paper 2000-01-1339**.

(5) Wang, L., Snidle, R. W., and Gu, L. (2000), "Rolling Contact Silicon Nitride Bearing Technology: A Review of Recent Research," *Wear*, **246**, pp 159-173.

(6) Piotrowski, A. E., and O'Brien, M. J. (2006), "A Novel Test Method to Measure the Fracture Toughness of Ceramic Balls Used in Bearings," *Fatigue and Fracture of Materials and Structures*, **29**, pp 558-572.

(7) Levesque, G., and Arakere, N. K. (2008), "An Investigation of Partial Cone Cracks in Silicon Nitride Balls," *International Journal of Solids and Structures*, **45**, pp 6301-6315.

(8) Zalounia, N. (1993), in *SIF Handbook*, Vol. 4, Murakami, Y. (Ed.), Pergamon Press, New York, pp 1110–1111.

(9) Keer, L. M., and Bryant, M. D. (1983), "A Pitting Model for Rolling Contact Fatigue," *Journal of Lubrication Technology*, **105**, pp 198-205.

(10) Karapetian, E. N., and Hanson, M. T. (1994), "Crack Opening Displacements and Stress Intensity Factors Caused by a Concentrated Load Outside a Circular Crack," *International Journal of Solids and Structures*, **31**(15), pp 2035-2052.

(11) Kida, K., and Ogura, K. (2000), "Fracture Mechanics Approach into the Flaking Subsurface Crack Growth of Si_3N_4 under Spherical Hertzian Rolling Contact," *JSME Transactions*, **66A**(644), pp 783-790.

(12) Hasebe, N., and Qian, J. (1995), "Circular Inclined Punch Problem with Two Corners to Contact with a Half Plane with a Surface Crack," in *Contact Mechanics II, Computational Techniques*, Computational Mechanics Publications: Southampton, pp 159-166.

(13) Qian, J., and Hasebe, N. (1999), "Cylindrical Rigid Punch Problem in Contact with a Half Plane with an Oblique Edge Crack," in *Computational Methods in Contact Mechanics IV*, Gaul, L. and Brebbia, C. A. (Eds.), WIT Press: Southampton, pp 140-151.

(14) Qian, J., and Hasebe, N. (1997), "Circular Rigid Punch on a Semi-Infinite Plane with an Oblique Edge Crack Subjected to Concentrated Forces or Point Dislocations," *Structurol Mechanics Earthquake Engineering*, **570**(40), pp 21-31.

(15) Qian, J., and Hasebe, N. (1996), "Fundamental Solutions of Circular Inclined Rigid Punch on a Half Plane with an Oblique Edge Crack," in *Boundary Element Technology XI*, Ertekin, R. C., Brebbia, C. A., Tanaka, M., and Shaw, R. (Eds.), Computational Mechanics Publications: Southampton, pp 125-135.

(16) Noda, N. A., and Miyoshi, S. (1996), "Variation of Stress Intensity Factor and Crack Opening Displacement of Semi-Elliptical Surface Crack," *International Journal of Fracture*, **75**(1), pp 19-48.

(17) Pommier, S., Sakae, C., and Murakami, Y. (1999), "An Empirical Stress Intensity Factor Set of Equations for a Semi-Elliptical Crack in a Semi-Infinite Body Subjected to a Polynomial Stress Distribution," *International Journal of Fatigue*, **21**, pp 243-251.

(18) Kaneta, M., and Murakami, Y. (1991), "Propagation of Semi-Elliptical Surface Cracks in Lubricated Rolling/Sliding Elliptical Contacts," *Journal of Tribology – Transactions of the ASME*, **113**(2), pp 270-275.

(19) Kaneta, M., Okazaki, T., and Murakami, Y. (1989), "Propagation of an Inclined Subsurface Crack in Rolling/Sliding Contact Fatigue," *Key Engineering Materials*, **33**, pp 191-212.

(20) Komvopoulos, K., and Cho, S. S. (1997), "Finite Element Analysis of Subsurface Crack Propagation in a Half-Space Due to a Moving Asperity Contact," *Wear*, **209**, pp 57-68.

(21) Zhang, H. Q., Sadeghipour, K., and Baran, G. (1999), "Numerical Study of Polymer Surface Wear Caused by Sliding Contact," *Wear*, **224**, pp 141-152.

(22) Kojima, Y. (1999), "Analysis of Rolling Contact Fatigue Crack Filled with Viscous Lubricating Oil," *Transactions of the Japan Society of Mechanical Engineers*, **65A**, pp 1337-1342.

(23) Warrier, S. G., Jarmon, D. C., and Chin, H. (2000), "Finite Element Analysis of the Critical Flaw Size in Hybrid Silicon Nitride Bearing Ball," *ASME Turbo Expo May 8–11 2000*, Munich, Germany.

(24) Fletcher, D. I., and Beynon, J. H. (1999), "A Simple Method of Stress Intensity Factor Calculation for Inclined Fluid-Filled Surface-Breaking Cracks under Contact Loading," *Proceedings of the Institution of Mechanical Engineers*, **213**, pp 299-304.

(25) Fletcher, D. I., and Beynon, J. H. (1999), "A Simple Method of Stress Intensity Factor Calculation for Inclined Surface-Breaking Cracks with Crack Face Friction under Contact Loading," *Proceedings of the Institution of Mechanical Engineers*, **213**, pp 481-486.

(26) Rooke, D. P., Rayaprolu, D. B., and Aliabadi, M. H. (1991), "Crack-Line and Edge Green's Functions for Stress Intensity Factors of Inclined Edge," *Fatigue and Fracture of Engineering Materials and Solids*, **15**(4), pp 441-461.

(27) Newman, J. C., and Raju, I. S. (1981), "An Empirical Stress-Intensity Factor Equation for the Surface Crack," *Engineering Fracture Mechanics*, **15**(2), pp 185-192.

(28) Levesque, G., and Arakere, N. K. (2010), "Critical Flaw Size in Silicon Nitride Ball Bearings," *Tribology Transactions*. **53**, pp. 511–519.

(29) Fracture Analysis Consultants. http://www.fracanalysis.com. FRANC3D/NG, ed. 5/9/09, Accessed 5/10/09
(30) Desault Systemes. (2007), *ABAQUS Theory Manual*, Dessault Systemes: Providence, RI.
(31) Anderson, T. L. (2005), *Fracture Mechanics: Fundamentals and Applications*, CRC Press: Boca Raton, FL.
(32) Aliabadi, M. H., and Rooke, D. P. (1991), *Numerical Fracture Mechanics*, Computational Mechanics Publications: Southampton, UK.
(33) Rice, J. R. (1968), "A Path Independent Integral and the Approximate Analysis of Strain Concentration by Notches and Cracks," *Journal of Applied Mechanics*, **35**, pp 379-386.
(34) Banks-Sills, L., Hershkovitz, I., Wawrzynek, P. A., Elias, R., and Ingraffea, A. R. (2005), "Methods for Calculating Stress Intensity Factors in Anisotropic Materials: Part I—z = 0 Is a Symmetric Plane," *Engineering Fracture Mechanics*, **75**(15), pp 2328-2358.
(35) Fujimoto, K., Ito, H., and Yamamoto, T. (1992), "Effect of Cracks on the Contact Pressure Distribution," *Tribology Transactions*, **35**(4), pp 683-695.
(36) Mackerle, J. (2001), "Finite Element and Boundary Element Analysis on Indentation Problems: A Biography (1997–2000)," *Finite Elements in Analysis and Design*, **37**, pp 811-819.
(37) Hadfield, M., Stolarski, T. A., Cundhill, R. T., and Horton, S. L. (1993), "Failure Modes of Ceramics in Rolling Contact," *Proceedings of the Royal Society of London - Series A*, **443**, pp 607-621.
(38) Wang, Y., and Hadfield, M. (2000), "The Influence of Ring Crack Location on the Rolling Contact Fatigue Failure of Lubricated Silicon Nitride: Experimental Studies," *Wear*, **243**, p 157.
(39) Zhao, P., Hadfield, M., Wang, Y., and Vieillard, C. (2006), "Subsurface Propagation of Partial Ring Cracks under Rolling Contact Part 1. Experimental Studies," *Wear*, **261**, p 382.